

# Detection of Forests Using Mid-IR Reflectance: An Application for Aerosol Studies

Yoram J. Kaufman and Lorraine A. Remer

**Abstract**—The detection of dark, dense vegetation is an important step in the remote sensing of aerosol loading. Current methods that employ the red (0.64  $\mu\text{m}$ ) and the near-IR (0.84  $\mu\text{m}$ ) regions are unsatisfactory in that the presence of aerosols in the scene distorts the apparent reflectance in the visible and near-IR ranges of the spectrum. The mid-IR spectral region is also sensitive to vegetation due to the absorption of liquid water in the foliage, but is not sensitive to the presence of most aerosols (except for dust). Therefore, mid-IR channels on the AVHRR and EOS-MODIS (e.g., the 3.75  $\mu\text{m}$  or the 3.95  $\mu\text{m}$  channels) have a unique potential for the remote sensing of dark, dense vegetation, particularly in the presence of biomass burning smoke or industrial/urban haze. The reflective part of the 3.75  $\mu\text{m}$  channel ( $\rho_{3.75}$ ) is applied to images of the AVHRR over the eastern United States. This channel was found to be correlated to reflectance at 0.64  $\mu\text{m}$  ( $\rho_{0.64}$ ), less sensitive to haze than the visible channel and superior to both the 0.64  $\mu\text{m}$  reflectance and the normalized difference vegetation index (NDVI) to determine forest pixels in an image. However, its application to monitor the seasonal evolution of vegetation is presently questionable. For the purpose of the remote sensing of aerosol over dark, dense vegetation, it is proposed that the dark, dense vegetation be determined from  $\rho_{3.75} < 0.025$ . These findings may have further implications for other specific applications of the remote sensing of vegetation in hazy atmospheres.

## I. INTRODUCTION

REMOTE sensing of vegetation including dark, dense vegetation (DDV) has focused on using the visible and near-IR parts of the spectrum. In this spectral range, the presence of vegetation decreases the reflectance of the Earth's surface in the red spectral band ( $\sim 0.65 \mu\text{m}$ ) due to absorption by chlorophyll in the process of photosynthesis, and increases the surface reflectance in the near-IR range due to backscattering from leaves and twigs [4]. Unfortunately, the red and near-IR channels are very sensitive to aerosol scattering and absorption in the atmosphere [3], [9] and these atmospheric effects impede remote sensing of vegetation. On the other hand, the mid-IR part of the spectrum, used extensively in the remote sensing of cloud properties [1], [2], [15], [20], [23] has not been widely applied to remote sensing of vegetation and the detection of DDV. Notable exceptions are the use of the 3.75  $\mu\text{m}$  channel on the NOAA Advanced Very

High Resolution Radiometer (AVHRR) to detect deforestation [22], [33] and the demonstration by Holben et al. [10] that 3.75  $\mu\text{m}$  radiance has the potential to detect DDV used in the remote sensing of aerosol and in atmospheric correction.

In this paper, we propose and test the application of a channel in the mid-IR, the 3.75  $\mu\text{m}$  channel on the AVHRR and MODIS satellites. Though the main purpose of the research is to develop methods for the remote sensing of dark, dense vegetation that are used to determine aerosol loading and perform atmospheric corrections [10], [16], the results suggest important implications for the remote sensing of vegetation in general. All reflectances described in this paper are the apparent reflectances observed by satellite unless otherwise noted.

## II. REMOTE SENSING OF VEGETATION

The main vegetation index used for the remote sensing of vegetation is the normalized difference vegetation index (NDVI):

$$\text{NDVI} = (\rho_{\text{NIR}} - \rho_{\text{red}}) / (\rho_{\text{NIR}} + \rho_{\text{red}}) \quad (1)$$

where  $\rho_{\text{NIR}}$  and  $\rho_{\text{red}}$  are the reflectances in the near-IR and red channels, respectively (e.g., channels 2 and 1 of the AVHRR). The NDVI has been linked to parameters such as vegetation cover, productivity, biomass, leaf area index, rainfall,  $\text{CO}_2$  variation, and so forth [6], [24], [28], [32], [34]. Though useful for these application, NDVI is also affected by atmospheric and surface properties not associated with photosynthetic activity of vegetation. These include the surface bidirectional reflectance [8], reflective properties of the background soil [11], and atmospheric effects—clouds, aerosols, and water vapor [8], [13]. Aerosols are of particular importance because the presence of aerosols distorts the apparent reflectance in the visible and near-IR range of the spectrum and alters the values of NDVI. Part of the atmospheric effect is reduced by compositing NDVI data over several consecutive images and choosing a value for each pixel that maximizes the vegetation index [8], [17], [30]. Further correction requires the determination of aerosol loading. This can be done by identifying pixels with dark vegetation using the NDVI itself [8] or the 3.75  $\mu\text{m}$  channel [10]. The determination of dark, dense vegetation is difficult using the NDVI itself because of the surface and atmospheric effects listed above.

Manuscript received February 2, 1993; revised December 2, 1993.

L. A. Remer is with Science Systems and Applications Inc., Lanham, MD 20706.

Y. J. Kaufman is with the Laboratory for Atmospheres, NASA Goddard Space Flight Center, Greenbelt, MD 20771.

IEEE Log Number 9400476.

Several suggestions have been proposed to combat the errors in NDVI. Huete [11] suggested a soil adjusted vegetation index (SAVI), which reduces the soil effects. Pinty and Verstraete [25] proposed the global environment monitoring index (GEMI), which reduces atmospheric effect. Kaufman and Tanré [19] developed the atmospherically resistant vegetation index (ARVI) for EOS-MODIS, which uses a blue channel to counteract the atmospheric effects in the red channel.

### III. REASONS TO EMPLOY THE MID-IR REGION

#### A. Surface Reflectance

There are several processes that make the mid-IR an interesting spectral range to detect dark, dense vegetation. We expect the reflective properties in the red and mid-IR to be correlated due to the simultaneous occurrence of processes that darken the surface in these two channels (Table I). An increase in the fraction of the surface covered by vegetation introduces chlorophyll that absorbs the solar radiation in the red part of the spectrum. However, active chlorophyll is associated with liquid water in the leaves, which absorb the solar radiation in the mid-IR. An increase in the soil moisture decreases the relative refractive index between the soil grains and the spaces between them, and thus increases the forward scattering by the grains and the ability to trap the red radiation. The same liquid water absorbs the radiation at  $3.75 \mu\text{m}$  and thus reduces the reflectivity of moist soils. Shadows introduced by vegetation or topography reduce the intensity of the reflected radiation in both spectral bands. These processes are not expected to result in the same reflectance in the red and mid-IR and there are other processes that may change the reflectance in the two channels.

Fig. 1 shows the spectral distribution of reflectance for various surfaces and the spectral distribution of the inverse of the absorption coefficient  $k$  for water. Table II lists the reflectances at  $3.75 \mu\text{m}$  for three types of leaves as well as tap water. The reflectance of the specific vegetation type is independent on leaf structure [4]. Overall, the reflectances tend to be lower than nonvegetative materials [27], [36] although for some soils, reflectances are much closer to vegetation values [21]. Another important factor in the physical process affecting the reflectance of radiation from plants is canopy structure. Absorption of photons are enhanced and reflectance reduced within plant canopies because incoming sunlight is trapped by the vertical structure [10]. The ability to trap photons depends on the plant canopy's depth, leaf area index, and leaf orientation. Photon trapping increases the separability among different vegetation classes. For example, in grasslands, leaves are mostly vertical, while in deciduous forests leaves are mostly horizontal and have a greater vertical depth. Thus, forests that are an example of dark, dense vegetation have a greater propensity to trap photons and will appear darker than surrounding grasslands in both the

TABLE I  
PROCESSES THAT REDUCE THE REFLECTIVITY OF THE RED AND MID-IR PARTS OF THE SPECTRUM

Process / channel	Red channel	Mid-IR channel
Increase of vegetation cover	Absorption by chlorophyll present in the leaves reduces the reflectance in this channel.	Absorption by liquid water, present in the leaves reduces the reflectance in this channel.
Increase of soil moisture	Presence of liquid water in the spacing between soil grains reduces the relative refractive index between the grains and the spaces, traps the radiation and reduces the reflectivity.	Absorption by the liquid water reduces the soil reflectance.
Presence of shadows	Reduces the reflectance.	Reduces the reflectance.

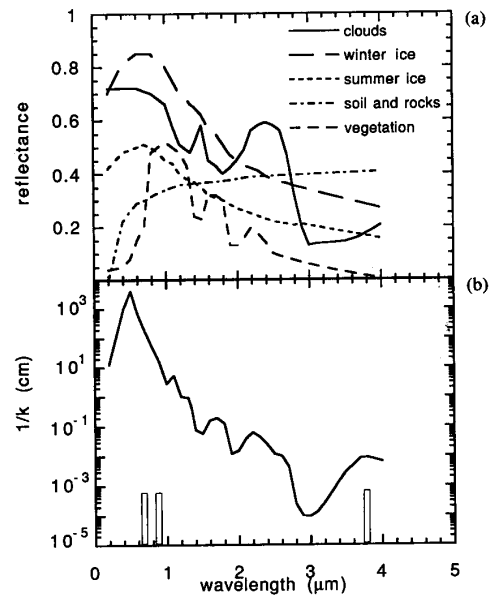


Fig. 1. (a) Spectral reflectances of several types of plants and soil surfaces and clouds after [36]. (b) Spectral distribution of the inverse of the absorption coefficient for water after [12].

TABLE II  
REFLECTANCE AT  $3.75 \mu\text{m}$  AND EMISSIVITY AT  $11 \mu\text{m}$  FOR THREE TYPES OF TREE LEAVES AND TAP WATER OF 6.3 mm DEPTH ON STEEL

	$\rho_{3.7}$	$\epsilon_{11}$
Black spruce	.005	.99
Sugar maple	.020	.94
Apple leaf	.035	.95
Tap water	.014	1.00

red and mid-IR, even if the leaves of the two vegetation classes have the same reflectance.

#### B. Atmospheric Effect

The main advantage of remote sensing in the mid-IR is the small ratio between the typical aerosol particle size (except dust) and the wavelength that decreases the at-

atmospheric opacity. The opacity of an aerosol layer can be described as a function of the Mie size parameter defined as

$$X = 2\pi r/\lambda \quad (2)$$

where  $r$  is the radius of the aerosol particle and  $\lambda$  the wavelength of incident radiation. Fig. 2 (after [7]) shows the scattering efficiency factor  $Q_s$  as a function of the Mie size parameter  $X$ .

For a typical aerosol particle from industrial or urban sources [35] or from smoke [18],  $r = 0.1\text{--}0.4\text{ }\mu\text{m}$ , and the values of  $X$  at  $\lambda = 0.64\text{ }\mu\text{m}$  and  $3.75\text{ }\mu\text{m}$  are  $X_{0.64} = 1.0\text{--}4.0$  and  $X_{3.75} = 0.17\text{--}0.67$ , respectively. In this range, the scattering efficiency varies as  $\sim X^2\text{--}X^3$ ; therefore the wavelength difference generates scattering efficiency that is 30–200 times smaller in  $\lambda = 3.75\text{ }\mu\text{m}$  than in  $\lambda = 0.64\text{ }\mu\text{m}$ . Therefore, using the  $3.75\text{ }\mu\text{m}$  channel has inherent advantages in that it better penetrates the haze layer for anthropogenic or organic smoke particles. On the other hand, for dust ( $r \sim 1\text{--}2\text{ }\mu\text{m}$ )  $X_{0.64} = 10\text{--}20$  and  $X_{3.75} = 17\text{--}3.4$ . In this case the atmospheric opacity in the mid-IR is larger than in the red channel (see Fig. 2), and using the mid-IR is no longer advantageous to determine DDV in the presence of this specific type of aerosol.

### C. Correction for Emission

Previous studies that used the AVHRR  $3.75\text{ }\mu\text{m}$  channel [10], [22], [33] employed the full radiance in this channel, including both the emissive and reflective parts, and thereby took advantage of the lower brightness temperatures of dark vegetation. This method works well regionally, in areas of flat topography where surface temperature gradients are mostly due to vegetative covers, but can backfire if applied globally, where temperature gradients are mostly due to latitudinal or topographic variations. On a global basis it is preferable to use the  $3.75\text{ }\mu\text{m}$  channel reflectance  $\rho_{3.75}$  and eliminate the emission component [5], [26].

To accomplish the correction for surface temperature emission we use the brightness temperature  $T$  from the  $11\text{ }\mu\text{m}$  channel.  $T$  is calculated by inverting the Planck function

$$L_{11} = t_{11}\epsilon_{11}B_{11}(T) \quad (3)$$

where  $L_{11}$  is the radiance measured in the  $11\text{ }\mu\text{m}$  channel,  $\epsilon_{11}$  is the emissivity,  $B_{11}$  is the Planck function, and  $t_{11}$  is the one-way atmospheric transmission in this channel. The radiance at the  $3.75\text{ }\mu\text{m}$  channel  $L_{3.75}$  consists of both an emissive part and a reflective part.

$$L_{3.75} = t'_{3.75}\rho_{3.75}\frac{F_0\mu_0}{\pi} + t_{3.75}\epsilon_{3.75}B_{3.75}(T) \quad (4)$$

where  $\rho_{3.75}$  is the reflectance in the  $3.75\text{ }\mu\text{m}$  channel,  $F_0$  is the incident solar radiance at the top of the atmosphere in the same spectral band and,  $\mu_0$  is the cosine of the solar zenith angle,  $\epsilon_{3.75}$  is the emissivity of the surface at  $3.75\text{ }\mu\text{m}$ ,  $B_{3.75}$  is the Planck function at  $3.75\text{ }\mu\text{m}$ , and  $T$  is the

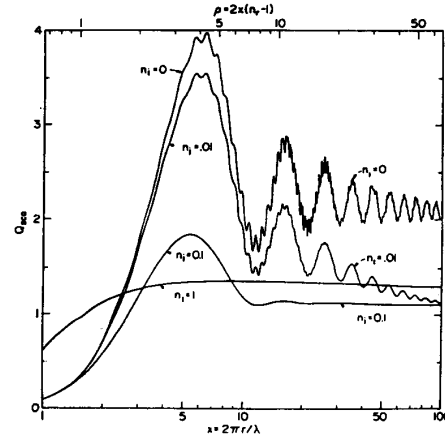


Fig. 2. Scattering efficiency factor  $Q_s$  as a function of Mie size parameter after [7]. The refractive index is  $m_r = 1.33$  with results shown for four values of  $m_i$ .

brightness temperature. The first term on the right-hand side describes the reflective part and the second term describes the emissive part.  $t'_{3.75}$  is the two-way transmission function and  $t_{3.75}$  is the one-way transmission function through the atmosphere in the  $3.75\text{ }\mu\text{m}$  band. Because the Earth's surface is not transparent, we can assume that  $\rho_{3.75} = 1 - \epsilon_{3.75}$  and rearrange (4) to solve for  $\rho_{3.75}$ . (Note that this assumption is exact for flux calculations and an approximation for radiances.)

$$\rho_{3.75} = \frac{L_{3.75} - t_{3.75}B_{3.75}(T)}{t'_{3.75}\frac{F_0\mu_0}{\pi} - t_{3.75}B_{3.75}(T)} \quad (5)$$

Gesell [5] and Ruff and Gruber [26] employ the above methodology and assume all transmission functions  $t_{11}$ ,  $t_{3.75}$ , and  $t'_{3.75}$ , as well as the emissivity  $\epsilon_{11}$  are equal to 1.0. Actually, the transmission functions depend on the temperature and water vapor in the atmospheric column, while the emissivity depends on surface properties. Sensitivity studies using simulations show that for a mid-latitude summer atmosphere in the vertical  $t_{11} = 0.97$ ,  $t_{3.75} = 0.92$ , and  $t'_{3.75} = 0.85$ , while for a tropical atmosphere  $t_{11} = 0.93$ ,  $t_{3.75} = 0.92$  and  $t'_{3.75} = 0.92$ . Emissivities of different natural substances have been measured in the laboratory and in the field. The long-wave emissivity at  $11\text{ }\mu\text{m}$  of leaves ranges from 0.94–0.99 with grass at the low end and deciduous trees at the high end of the range [4]. For soils, the emissivity is dependent on soil composition and moisture content [27]. For dry soils of mixed clay, silt, and sandy composition the emissivity is near 0.94–0.97 [21], [27]. In reality, the emissivity of soils mapped in the field in the eastern United States have a much higher moisture content and exhibit higher emissivities (0.96–0.99) [31].

Fig. 3 shows the sensitivity of  $\rho_{3.75}$  as given by (5) to different assumptions of transmission functions and surface emissivity as a function of temperature. In all plots, the solid curve represents the assumption that  $\epsilon_{11}$ ,  $t_{11}$ ,  $t_{3.75}$ ,

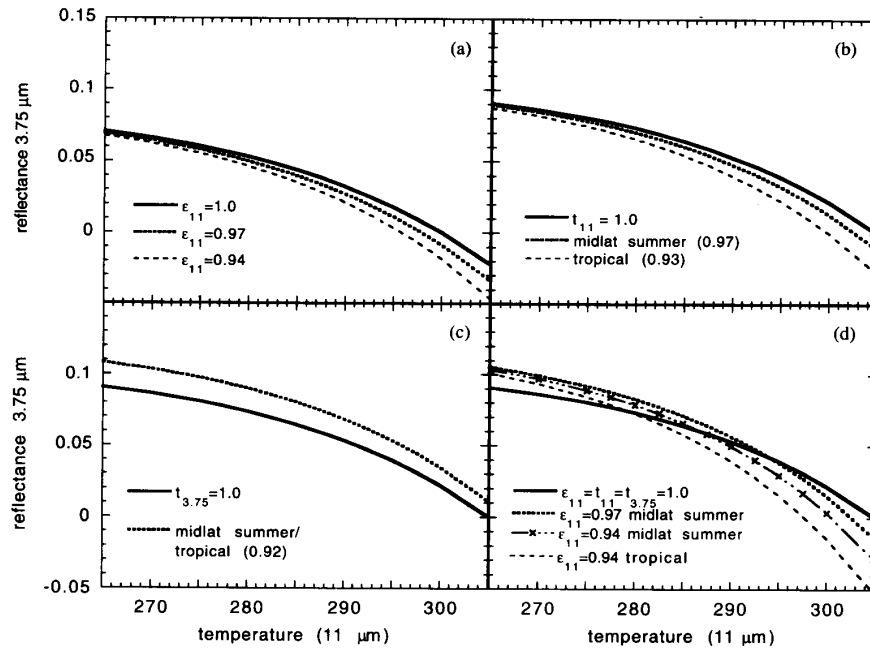


Fig. 3. Sensitivity of the temperature (11  $\mu\text{m}$ ) derived reflectance at 3.75  $\mu\text{m}$ ,  $\rho_{3.75}$ , to assumptions of (a) emissivity at 11  $\mu\text{m}$ ,  $\epsilon_{11}$ , (b) transmissivity at 11  $\mu\text{m}$ ,  $t_{11}$ , (c) transmissivity at 3.75  $\mu\text{m}$ ,  $t_{3.75}$ , and (d) combinations of the three variables for different values of 11  $\mu\text{m}$  brightness temperature. The solid curve in each case refers to the assumption that  $\epsilon_{11} = t_{11} = t_{3.75} = 1.0$ .

and  $t'_{3.75}$  are equal to 1.0, following Gesell [5] and Ruff and Gruber [26]. In Fig. 3(d) we see that for a mid-latitude atmosphere over a surface with  $\epsilon_{11} = 0.97$  (deciduous trees), the assumption of Ruff and Gruber [26] deviates by less than 0.013 in reflectance units. An uncertainty this small is manageable.

However, for a mid-latitude atmosphere in the range of emissivities expected by a variety of vegetation and soils (0.94–1.0) the uncertainty increases to the point that it nearly equals the value of  $\rho_{3.75}$ . Looking at each parameter individually we see that the assumption of  $\epsilon_{11} = 1.0$  and  $t_{11} = 1.0$  are conservative assumptions in that the emission-corrected  $\rho_{3.75}$  will be greater than or equal to the actual reflective part of this channel. In searching for dark, dense vegetation, we may miss pixels that would otherwise qualify for the threshold, but we are assured that all of the pixels that we do identify are indeed dark at 3.75  $\mu\text{m}$ . The assumption of  $t_{3.75} = 1.0$  works in the opposite way. However, in the range of temperatures expected of a mid-latitude summer ( $T > 290$  K) the overall effect of assuming that all parameters are equal to 1.0 remains conservative [Fig. 3(d)]. In this paper we analyze a series of AVHRR images collected during the summer on the eastern coast of the United States. Because of the season and location of our data set, we choose the conservative assumption of parameters in the correction for emission. There may be other applications of the mid-IR in which different assumptions of emissivity and transmissivities are more appropriate.

The error introduced by correcting for emission is reasonably small and can either be mitigated by a practical

choice of parameters or used to our advantage in order to identify dark vegetation pixels. In the remainder of this paper we have chosen to follow previous studies and use the simpler, more conservative, upper-bound assumption for emissivity and transmission functions (i.e.,  $\epsilon_{11} = t_{11} = t_{3.75} = t'_{3.75} = 1.0$ ).

#### IV. APPLICATION TO THE AVHRR

In this section the properties of  $\rho_{3.75}$ ,  $\rho_{0.64}$ , and NDVI will be compared using AVHRR data. Two sites in the mid-Atlantic region of the eastern United States were selected for intensive study of several AVHRR images of 1 km resolution. The sites were chosen with the aid of U.S. Geological Survey 7.5 min series topographical maps, where the scale is 1:24 000. These maps, photo revised in 1983, provide contours of the topographical elevation and also indicate roads, buildings, bodies of water, and forested areas. The first site spans the Maryland/Delaware border, encompassing approximately 660  $\text{km}^2$  of flat terrain, covered in part by patches of forest of limited extent, but also including an area that is mostly unforested and another 80  $\text{km}^2$  area that is designated as a forested swamp. The second site is in southeastern Pennsylvania and encompasses 825  $\text{km}^2$  of complex terrain. This site includes sections of Blue Mountain, Stony Mountain, and Second Mountain, which reach elevations of over 500 m. The maps indicate that these mountains are all forested. The lowlands adjacent to the mountains are unforested rolling hills that could be vegetated either with crops or pasture or be exposed bare soil. From the topographic maps we are only able to distinguish between

TABLE III  
VISIBILITY (KILOMETERS) AND RELATIVE HUMIDITY REPORTED BY NEARBY METEOROLOGICAL STATIONS AT THE TIME OF SATELLITE OVERPASS FOR EACH OF THE AVHRR IMAGES USED IN THIS ANALYSIS. 4/21/87 IS NOT AVAILABLE

DATE	Visibility (km)		Humidity (%)	
	MD/DE	PA	MD/DE	PA
5/9/87	28	30	30	32
5/10/87	25	25	29	32
6/5/87	20	30	50	29
6/6/87	20	30	43	33
6/24/87	20	23	54	44
6/25/87	18	23	52	40
7/5/87	19	38	57	43
7/21/87	07	19	47	47
7/22/87	18	30	50	35
7/23/87	16	38	47	37
8/20/87	22	42	36	39
8/21/87	25	45	35	31

forests and open areas, and cannot determine other vegetative characteristics.

Agricultural authorities for Berks County, Pennsylvania estimate that approximately 40 percent of the non-forested, open land at our Pennsylvania site is cultivated. The remainder of this land is either pasture or undeveloped. The crops are a mixture of corn and soybeans that are planted in plowed fields during late May and June and winter wheat and barley that are planted in the fall, grow green in the spring, turn brown in June, and are harvested in July. Late corn or soybeans may be planted in the empty wheat fields after the July harvest.

Because there is a general relationship between inverse invisibility and aerosol optical thickness [14], and because water vapor absorption affects the reflectance at the AVHRR 0.84 and 3.75  $\mu\text{m}$  channels, the visibilities and relative humidities recorded at nearby meteorological stations are listed in Table III. The reciprocal of the visibilities, which is a measure of the optical thickness, are plotted in Fig. 4 for the Pennsylvania site. These will be used for atmospheric correction of the visible reflectances in subsequent sections.

Thirteen images of AVHRR data were used in the analysis, but the Maryland/Delaware site was cloud free in only three of the images. These images span the growing season in 1987 and were chosen because the sites were viewed from an angle less than 30° from the nadir of the satellite and the area was relatively cloud free. The images were registered by translation after aligning the image with the coastlines of southern New Jersey, including Cape May and eastern Delaware. Images with a great amount of rotation were not included. The Maryland/Delaware (MD/DE) site is only 20 km from the registration coastline and the Pennsylvania (PA) site is roughly 150 km away. The registration was accomplished with as much accuracy as possible; however, each image remains slightly distorted and the accuracy of the registration is expected to be within 3–5 km.

Cloudy pixels, detected by a ratio of the 0.84  $\mu\text{m}$  channel to the 0.64  $\mu\text{m}$  channel of less than 1.2 or 11  $\mu\text{m}$  channel temperature less than a specific threshold for each day and each site, were discarded. Every effort was made

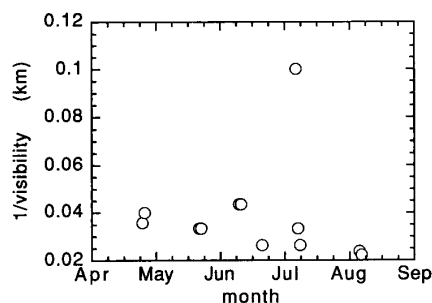


Fig. 4. Measure of optical thickness for the PA site calculated as 1/visibility where visibilities are those measured by nearby meteorological stations.

to be liberal in detecting clouds. We wanted to be as sure as possible that pixels were indeed cloud free. However, we cannot be certain that the pixels are completely uncontaminated by subpixel clouds. For each image, each pixel determined to be cloud free was located on the topographic maps by its registered latitude and longitude, then categorized as to whether it was forest, open field, mixed forest with open field, or urban. Depending on cloudiness, 400–800 pixels are ready for analysis at each site. Roughly half the pixels are categorized as open field, a fourth are forest, a fourth mixed, and only a handful are urban.

## V. SPATIAL ANALYSIS

We first investigate the relationship between the spatial variability of  $\rho_{3.75}$  and  $\rho_{0.64}$ , image by image. Fig. 5 shows the relationship between  $\rho_{3.75}$  and  $\rho_{0.64}$  for all categories of pixels at the MD/DE and PA sites for selected days. In all six plots we see an agreement with our basic premise that a strong relationship exists between the reflectances in the two channels. Correlation coefficients range between 0.74 and 0.96. These results imply that in any particular image remote sensing of vegetation with  $\rho_{3.75}$  is possible and will still provide the advantage of being able to penetrate most types of hazy atmospheres.

## VI. SEPARATION BETWEEN FOREST AND NONFOREST PIXELS

The data points plotted in Fig. 5 designate the category of land cover by using different symbols. The x's or +'s denote forest and the open circles denote open land, which may be agricultural crops, pasture, or bare soil. Urban areas are denoted with a filled circle. In some plots only forest and open pixels are denoted. In these figures and in subsequent discussion we consider the forest category to be the dark, dense vegetation that is the object of our analysis. In Fig. 5 we see a separation between the forest pixels and the open pixels in both the 0.64  $\mu\text{m}$  channel reflectance and the 3.75  $\mu\text{m}$  channel reflectance. Forests are darker at both wavelengths. There were few urban areas in our test sites, but the pixels with urban land cover tended to be some of the brightest pixels in both channels.

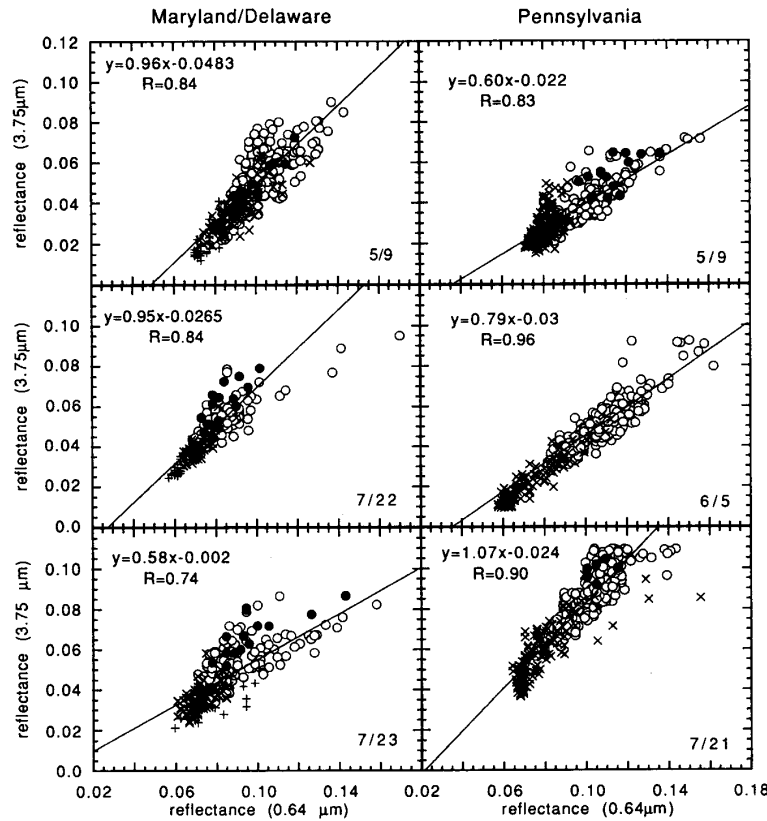


Fig. 5. Scatter diagrams of reflectance at  $3.75 \mu\text{m}$  versus reflectance of  $0.64 \mu\text{m}$ . Each point represents a pixel from an AVHRR image for a site located on the Maryland/Delaware border (MD/DE) or in southeastern Pennsylvania (PA). Forest pixels are denoted by X's, forested swamps by +', open fields by o's, and urban areas by filled circles. The line indicates the linear regression between the two reflectances for each image. The regression and correlation coefficients are given for each graph.

There is some scatter and some overlap, especially at the MD/DE site, where the areas of forest are smaller and more interspersed with the open areas. Slight inaccuracies in the registration of the satellite image would affect the classification of pixels at the MD/DE site more than it would affect the PA site, where there are larger expanses of forests and open land.

A comparison of the ability of the red, mid-IR, and NDVI to separate between forest pixels and nonforest pixels is shown in the histograms of Fig. 6. June 5 at the PA site is a relatively easy image to make a separation between forest and open pixels. Any of the variables will make the separation. July 22 at the MD/DE site is a much more difficult image to separate forest pixels from open pixels. The  $3.75 \mu\text{m}$  reflectance does somewhat better than the other variables. Similar histograms were performed for all the locations and images.

In order to quantify the histogram's separation we define a measure

$$M = \frac{\text{mean}_{\text{forest}} - \text{mean}_{\text{open}}}{\sigma_{\text{forest}} + \sigma_{\text{open}}} \quad (6)$$

which is the difference in the means of the forest and open histograms normalized by the sum of the standard devia-

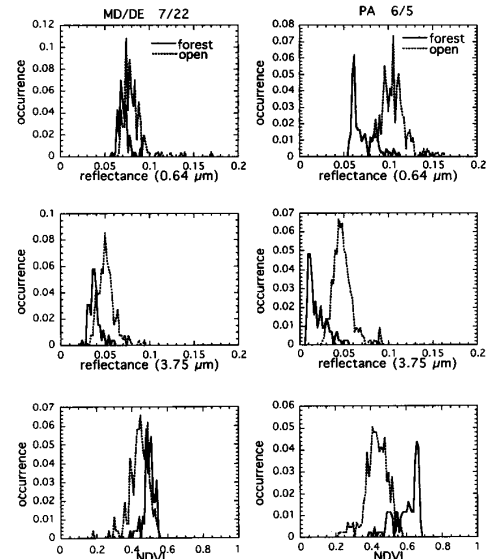


Fig. 6. Histograms of reflectance at  $0.64 \mu\text{m}$ , reflectance at  $3.75 \mu\text{m}$ , and NDVI. MD/DE, July 21 on the left-hand-side. PA, June 5 on the right-hand-side. Solid line denotes the histogram of forest pixels and dotted line denotes the histogram of open land pixels. Histograms are normalized by the total number of pixels in the combined population.

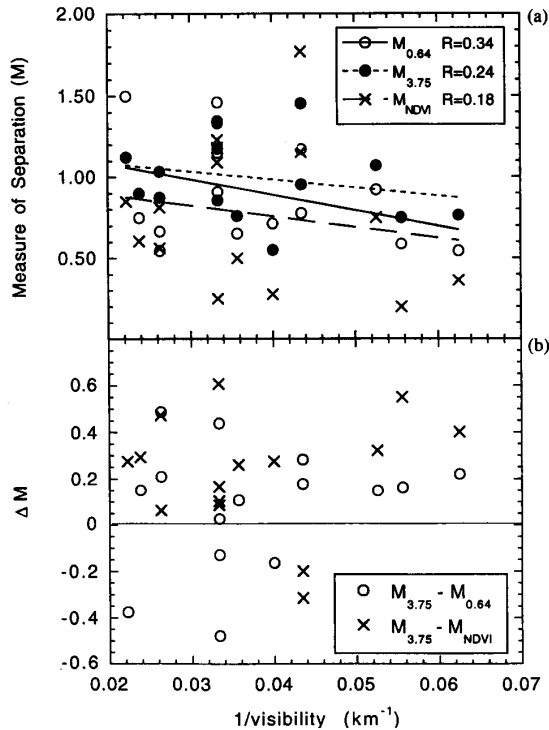


Fig. 7. (a) The measure of separation  $M$  between histograms of forest pixels and histograms of open land pixels plotted as a function of  $1/\text{visibility}$ .  $M$  is the difference in the means of the forest and open land histograms normalized by the sum of the histograms' standard deviations. The lines indicate the least-square fit for each variable. (b) The difference in the separability between  $\rho_{3.75}$  and NDVI (x's) and,  $\rho_{3.75}$  and  $\rho_{0.64}$  (circles).

tions. The same difference in means will give different measures of separability depending on the spread of the histograms. Wider histograms (larger  $\sigma$ 's) will cause more overlap and less separability than narrow histograms (smaller  $\sigma$ 's) for the same difference in means. Using  $M$  we can compare the three quantities,  $\rho_{0.64}$ ,  $\rho_{3.75}$ , and NDVI in their ability to separate forest pixels from open land pixels.  $M > 1.0$  indicates good separation, while  $M < 1.0$  indicates poor separation.

For the two examples in Fig. 6,  $M = 1.5$ ,  $1.3$ , and  $1.2$  for  $\rho_{0.64}$ ,  $\rho_{3.75}$ , and NDVI of 6/5, respectively, while  $M = 0.6$ ,  $0.8$ , and  $0.5$  for  $\rho_{0.64}$ ,  $\rho_{3.75}$ , and NDVI of 7/22, respectively. Thus we see overall larger values of  $M$  for 6/5 than for 7/22 because it is easier overall to make a separation on 6/5. On 7/22, where the separation is more difficult, the quantity  $\rho_{3.75}$  gives the highest measure of separability.

Fig. 7(a) plots  $M$  as a function of  $1/\text{visibility}$  in kilometers $^{-1}$  for each of the analyzed images.  $1/\text{visibility}$  is a rough measure of the haziness. Open circles denote  $M$  using  $\rho_{0.64}$  ( $M_{0.64}$ ), filled circles show  $M$  using  $\rho_{3.75}$  ( $M_{3.75}$ ) and x's represent  $M$  using NDVI ( $M_{\text{NDVI}}$ ). The mean value of  $M_{3.75}$  is 1.0,  $M_{0.64}$  is 0.9, and  $M_{\text{NDVI}}$  is 0.8, suggesting that  $\rho_{3.75}$  is a better separator of forest pixels from open land pixels than the two other quantities. Also plotted in Fig. 7(a) are the curves of linear least-square fits of the

respective data points. There is much scatter in the data, making the correlation coefficients for  $M_{0.64}$ ,  $M_{3.75}$ , and  $M_{\text{NDVI}}$  only 0.34, 0.24, and 0.18, respectively. However these lines do show that on average  $M_{3.75} > M_{0.64} > M_{\text{NDVI}}$ .

Fig. 7(b) shows the difference between  $M$ 's using  $\rho_{3.75}$  (open circles) and  $\rho_{3.75}$  and NDVI (x's). Positive quantities denote that there is a greater separation between forest and open land histograms using  $\rho_{3.75}$ . Open circles below the zero-line indicate that  $\rho_{0.64}$  is a better quantity to use for separating histograms and x's below the zero-line indicate that NDVI is a better separator. In most cases the points reside above the zero-line, demonstrating that  $\rho_{3.75}$  is the best quantity to use to separate forest pixels from open land pixels in our images. Note that in most cases where  $\rho_{3.75}$  fails to provide the *best* separation of the three quantities such as 6/5 in Fig. 6, any of the three quantities are good separators. However, in the difficult cases such as 7/22 in Fig. 6,  $M_{3.75}$  tends to be larger than  $M_{0.64}$  or  $M_{\text{NDVI}}$ . Note also that for the three highest haze values (largest  $1/\text{visibility}$ )  $M_{3.75}$  always exceeds  $M_{0.64}$  and  $M_{\text{NDVI}}$ . Three images are far too few to draw conclusions. However, there is the suggestion that  $\rho_{3.75}$  is more useful in separating forest pixels from open land pixels in thicker haze. This point will be emphasized in theoretical analysis in Section VIII.

## VII. TEMPORAL ANALYSIS

Fig. 8 shows the seasonal evolution over the course of a growing season of  $\rho_{0.64}$  (x's),  $\rho_{3.75}$  (filled circles), and also  $\rho_{s0.64}$ , the surface reflectance corrected for atmospheric effects using observed surface visibilities (Table III) and denoted by (+'s) in the figure. The correction procedure is described in Section IX. Mean values of each variable are plotted for the two surface classifications of open and forest pixels. Mean values and standard deviations are given for all variables in Table IV.

In these figures we see the response of the remote sensing variables to the increase in vegetation as the forests produce leaves and the open spaces sprout grass and cultivated crops. For the forest pixels,  $\rho_{0.64}$ ,  $\rho_{s0.64}$ , and  $\rho_{3.75}$  decrease through the spring and somewhat level off during midsummer. The darkening through the spring is much more evident for the visible channel than for the mid-IR.  $\rho_{3.75}$  appears to reach its low summer value as early as May, while it takes  $\rho_{0.64}$  and  $\rho_{s0.64}$  until early June to reach the dark summer values. This implies that  $3.75 \mu\text{m}$  radiation is more sensitive to absorption by liquid water in vegetation than  $0.64 \mu\text{m}$  radiation is to absorption by plant pigments. In the open fields the visible channels continue to darken even through the summer, while  $\rho_{3.75}$  does not show a definite seasonal trend.

The data were analyzed with respect to temperature, humidity, visibility, precipitation, as well as solar and satellite angles. Other than a weak relationship with temperature,  $\rho_{3.75}$  was found to be independent of these other variables. July 21, 22, and 23 appear to have unseason-

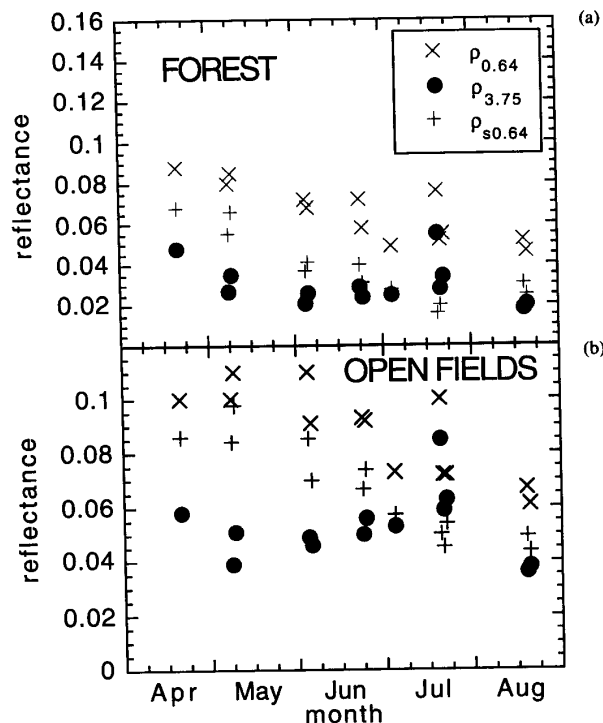


Fig. 8. Seasonal evolution of  $\rho_{0.64}$  (x's), the atmospherically corrected value of the visible reflectance:  $\rho_{0.64}$  (+s) and  $\rho_{3.75}$  (closed circles) for the PA site during 1987. (a) Represents only forest pixels. (b) Represents only open fields. Plotted are the mean values for each subpopulation of the pixels for the image indicated.

ably high values of  $\rho_{3.75}$  in Fig. 8. These three days are also the warmest of all the days analyzed. There is insufficient data to determine whether  $\rho_{3.75}$  is directly or indirectly dependent on temperature or whether the higher temperatures for those three days in July are an unrelated coincidence. One possible explanation for  $\rho_{3.75}$ 's temporal inconsistencies with  $\rho_{0.64}$  might be temporal variations of surface emissivity, which would affect  $\rho_{3.75}$  in the correction for emission. For example, if the surface emissivity  $\epsilon_{11}$  for the open pixels was 0.96 on July 21, 22, and 23 but remained 1.0 on the other dates, the mean value of  $\rho_{3.75}$  for the three dates in July would drop to 0.054 from the previous value of 0.069. A seasonal or day-to-day variation of  $\epsilon_{11}$ , related or unrelated to temperature, can create variations in  $\rho_{3.75}$  large enough to explain the temporal inconsistencies with  $\rho_{0.64}$ .

The significance of Fig. 8 is not that  $\rho_{0.64}$  and  $\rho_{3.75}$  change with season but that they change at different rates. Fig. 5 shows that  $\rho_{0.64}$  is highly correlated to  $\rho_{3.75}$  in each image, but Fig. 8 implies that the relationship between the variables changes from image to image. This can be better seen in the variation of the linear regression equations calculated for each image. Fig. 9 shows a plot of the slope of each linear regression equation calculated for each image and distinguished by surface type. For the open fields, we see higher slopes in the latter part of the growing season than in the beginning. We do not know

TABLE IV  
MEAN AND STANDARD DEVIATION OF THE FOREST PIXELS AND THE OPEN LAND PIXELS FOR THE REFLECTANCES AT 0.64, 0.84, AND 3.75  $\mu\text{m}$ , FOR THE BRIGHTNESS TEMPERATURE AT 11  $\mu\text{m}$ , AND NDVI AND VI3 FOR EACH ANALYZED SITE AND IMAGE. REFLECTANCES IN PERCENT

		$\rho_{0.64}$	$\rho_{0.84}$	$\rho_{3.75}$	T( $^{\circ}\text{K}$ )	NDVI	VI3
<b>Forest</b>							
MD/DE	5/9	8.6 (1.1)	20.0 (1.2)	3.2 (1.2)	297 (1.3)	0.40 (0.05)	0.73 (0.09)
	7/22	6.8 (0.7)	21.3 (1.2)	3.6 (0.7)	299 (1)	0.51 (0.04)	0.71 (0.05)
	7/23	7.3 (0.8)	19.3 (2.1)	3.6 (0.7)	299 (1)	0.45 (0.06)	0.69 (0.05)
PA	4/21	8.8 (0.7)	19.0 (2.0)	4.8 (0.5)	298 (0.5)	0.36 (0.04)	0.59 (0.04)
	5/9	8.0 (0.5)	19.5 (1.4)	2.7 (0.7)	295 (2)	0.41 (0.04)	0.76 (0.06)
	5/10	8.5 (1.7)	19.0 (4.2)	3.5 (1.3)	298 (1.2)	0.38 (0.07)	0.69 (0.07)
	6/5	7.2 (1.3)	29.0 (2.1)	2.1 (1.0)	297 (1.8)	0.60 (0.07)	0.86 (0.07)
	6/6	6.8 (0.8)	24.0 (1.4)	2.6 (0.8)	297 (1.6)	0.56 (0.05)	0.80 (0.06)
	6/24	7.2 (1.5)	26.0 (2.1)	2.9 (1.2)	297 (1.5)	0.56 (0.08)	0.80 (0.08)
	6/25	5.8 (0.8)	23.0 (2.0)	2.4 (0.8)	297 (1.3)	0.59 (0.05)	0.81 (0.06)
	7/5	4.9 (1.5)	26.0 (2.1)	2.9 (1.2)	297 (1.5)	0.56 (0.08)	0.80 (0.08)
	7/21	7.6 (1.3)	26.0 (2.9)	5.5 (1.3)	299 (2)	0.55 (0.07)	0.65 (0.09)
	7/22	5.2 (1.0)	23.2 (1.8)	2.8 (0.8)	301 (2)	0.64 (0.05)	0.78 (0.06)
<b>Open Land</b>	7/23	5.5 (1.5)	19.8 (3.3)	3.4 (1.3)	300 (2)	0.56 (0.09)	0.71 (0.10)
	8/20	5.2 (0.7)	19.0 (2.8)	1.8 (0.7)	296 (1.6)	0.58 (0.06)	0.83 (0.06)
	8/21	4.6 (0.4)	18.0 (1.3)	2.0 (0.6)	297 (1.1)	0.58 (0.04)	0.80 (0.06)
	5/9	10.1 (1.2)	20.1 (1.5)	5.1 (1.3)	299 (1.1)	0.33 (0.05)	0.60 (0.09)
	7/22	7.8 (1.0)	21.6 (1.1)	4.8 (0.9)	300 (0.6)	0.49 (0.05)	0.64 (0.06)
	7/23	8.5 (1.4)	20.1 (1.8)	4.9 (1.0)	299 (1.2)	0.41 (0.06)	0.61 (0.06)
	4/21	10.0 (1.8)	18.0 (2.6)	5.8 (1.2)	298 (1.1)	0.28 (0.05)	0.51 (0.05)
	5/9	10.3 (1.0)	23.8 (1.5)	4.0 (0.7)	297 (0.7)	0.40 (0.04)	0.71 (0.05)
PA	5/10	11.0 (1.8)	22.0 (3.5)	5.1 (1.6)	297 (1.5)	0.34 (0.06)	0.62 (0.06)
	6/5	11.0 (1.3)	27.0 (1.3)	4.9 (1.1)	300 (1.0)	0.44 (0.06)	0.69 (0.07)
	6/6	9.1 (1.2)	23.0 (1.0)	4.6 (0.9)	299 (1.1)	0.44 (0.06)	0.67 (0.06)
	6/24	9.3 (1.2)	22.0 (1.1)	5.0 (1.0)	300 (1.1)	0.41 (0.05)	0.63 (0.06)
	6/25	9.2 (2.1)	19.0 (3.0)	5.6 (1.4)	300 (2.1)	0.36 (0.08)	0.55 (0.07)
	7/5	7.3 (2.1)	26.0 (2.1)	5.3 (2.0)	299 (1.8)	0.48 (0.08)	0.60 (0.11)
	7/21	10.0 (1.3)	27.0 (1.9)	8.5 (1.5)	300 (2)	0.46 (0.05)	0.52 (0.07)
	7/22	7.2 (1.2)	22.0 (1.5)	5.9 (1.5)	304 (2)	0.51 (0.06)	0.58 (0.09)
	7/23	5.5 (1.6)	19.8 (2.0)	6.3 (1.5)	302 (2)	0.47 (0.07)	0.52 (0.09)
	8/20	6.7 (1.3)	20.0 (3.6)	3.6 (1.3)	299 (1.7)	0.49 (0.08)	0.69 (0.09)
	8/21	6.1 (0.6)	18.0 (1.6)	3.8 (1.0)	300 (1.4)	0.50 (0.06)	0.66 (0.09)

the cause of this change, although variations in surface emissivity are among the possibilities. The reflectances of the forest pixels are often concentrated in clumps of pixels rather than a line. Therefore, the ratio of the reflectances  $\rho_{3.75}$  to  $\rho_{0.64}$  was plotted instead. The ratios vary but do not appear to evolve with season for the forest pixels.

Although the data supports our basic premise that  $\rho_{3.75}$  is well correlated to  $\rho_{0.64}$ , the relationship between these variables changes from image to image over the course of a growing season. This may be due to changes in the surface emissivity at 11  $\mu\text{m}$  or it may simply point out that although both the mid-IR and the visible spectral regions measure vegetation, the two spectral regions measure different vegetation phenomena. In either case, there is no detractor from the mid-IR's superiority in detecting dark, dense vegetation in a single image.

#### VIII. SIMULATION OF THE EFFECT OF AEROSOL AND WATER VAPOR ON $\rho_{0.64}$ AND $\rho_{3.75}$

We employ the 5S radiative transfer model [29] to test the sensitivity of  $\rho_{0.64}$  and  $\rho_{3.75}$  to visibility (optical thickness) variations. As a preparation the model is run for mid-latitude summer conditions for a mixture of 74 percent water-soluble particles, 23 percent dust-like particles, and 3 percent soot with visibilities equal to 30 km



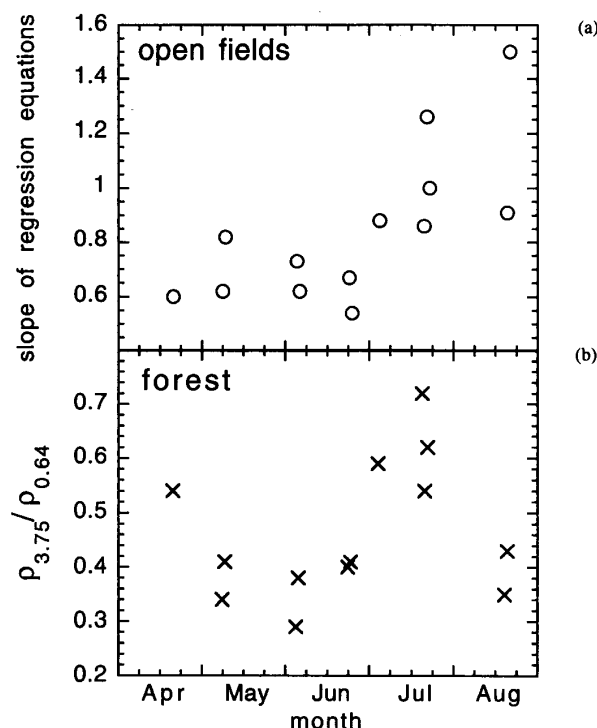


Fig. 9. (a) Seasonal evolution of slopes of the linear regression equations calculated for scatter diagrams of  $\rho_{3.75}$  versus  $\rho_{0.64}$  for open field pixels (open circles) for the PA site. (b) Seasonal evolution of ratios between  $\rho_{3.75}$  and  $\rho_{0.64}$  for forest pixels at the PA site.

as well as for a mixture of 91 percent water-soluble particles, 5 percent dust-like particles and 4 percent soot for a visibility of 5 km. The surface reflectances were equal to 0.0 and 0.2 for the AVHRR channels 1 and 2 (integrated about  $\lambda = 0.64 \mu\text{m}$  and  $0.84 \mu\text{m}$ , respectively) in addition to a box function representing the  $3.75 \mu\text{m}$  channel with band cutoffs at  $3.59 \mu\text{m}$  and  $3.98 \mu\text{m}$ . The result of each model run is the apparent reflectance received at the satellite approximated by

$$\rho_i = \rho_{oi}(V) + \rho_{si} * T_i(V) \quad (7)$$

where  $\rho_i$  is the apparent reflectance at the satellite for wavelength  $i$ .  $\rho_{oi}(V)$  is the path radiance normalized by the solar flux for a given visibility.  $\rho_{si}$  is the surface reflectance and  $T_i(V)$  is the transmittance at a given visibility  $V$  and the wavelength  $i$ . We use the model results to solve for  $\rho_{oi}(V)$  and  $T_i(V)$ . Using (7) assuming a linear relationship between  $\rho_{oi}$ ,  $T_i$ , and optical thickness, and an inverse relationship between the optical thickness and visibility [14] we interpolated  $\rho_{oi}$  and  $T_i$  for any visibility. The visibilities are listed in Table III. Thus, given the measured apparent reflectance  $\rho_i$  and the reported visibility we can determine the surface reflectance  $\rho_{si}$ . From  $\rho_{si}$  the apparent reflectance ( $\rho_i$ ) can be calculated for any visibility.

We use this method to calculate the surface reflectances for a chosen AVHRR transect across the PA site on June

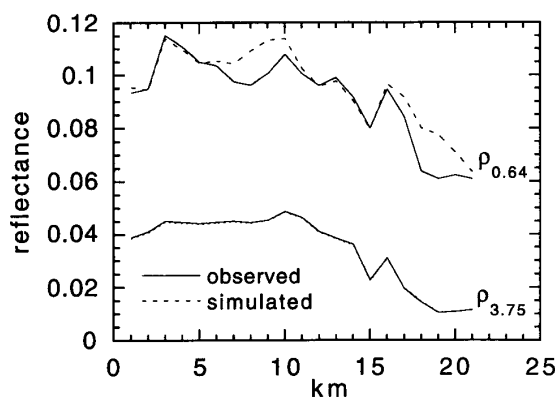


Fig. 10. Transect of PA site showing the values of  $\rho_{0.64}$  and  $\rho_{3.75}$  as a function of distance along the transect. The solid curves denote the observed AVHRR values. The dashed curves denote the values resulting from a simulation using the 5S radiative transfer model with a sinusoidally varying visibility. Visibility ranges from 10 to 35 km with a period equal to one half the transect length.

6, 1987. Next, we introduce a sinusoidal variation of visibilities across the transect with a period equal to half the length of the transect. Visibilities range from 10 to 35 km. We interpolate  $\rho_{oi}$  and  $T_i$  to correspond to each given visibility and use (7) to calculate the apparent reflectance at the satellite at each pixel in the transect. Calculations are made for the  $0.64$  and  $3.75 \mu\text{m}$  channels.

Fig. 10 shows the results. The solid curves denote the observed values of each variable. The dashed curves denote the calculated values of the apparent reflectance subjected to the spatial variability of visibility. The two curves should meet at visibility equal to 30 km, the recorded value at the time of observation (Table III). As visibilities deviate from 30 km the calculated values for  $\rho_{0.64}$  differ from the observed values. In the case of  $\rho_{3.75}$  there is negligible difference between the observed and calculated reflectances for the entire range of visibilities. Fig. 10 is a clear demonstration, though based on an atmospheric model, of the insensitivity of  $\rho_{3.75}$  to changes in visibility (or optical thickness) and the advantages  $\rho_{3.75}$  has in hazy conditions.

#### IX. APPLICATION TO REMOTE SENSING OF AEROSOL LOADING

The main method of remote sensing of aerosol loading over land requires the identification of dark dense vegetation and the estimation of the surface reflectance of this vegetation in the visible [16]. In the previous sections we have shown that  $\rho_{3.75}$  provides a better means of separating forest pixels from open land pixels and that  $\rho_{3.75}$  is less sensitive to haze than  $\rho_{0.64}$ .

We assume that the population of forest pixels in our study represents dark, dense vegetation and use the mean values of this population to define threshold values in  $\rho_{3.75}$ . However, we exclude the days of April 21 and July 21 in calculating this mean because  $\rho_{3.75}$  on those days appears to be anomalously high (Fig. 8) and we want the thresh-

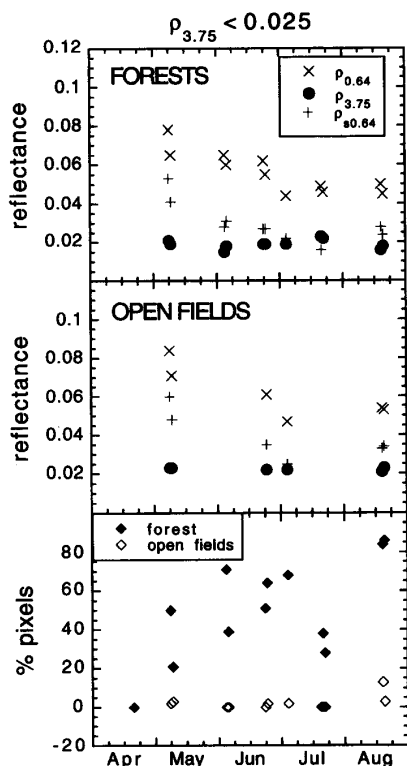


Fig. 11. Mean values of  $\rho_{0.64}$  (x's),  $\rho_{s0.64}$  (+s) and  $\rho_{3.75}$  (closed circles) calculated from the pixels that passed the threshold test of  $\rho_{3.75} < 0.025$  separated by surface category: forests or open fields. Also plotted in the bottom frame are the percentages of pixels, forests denoted by filled diamonds, and open fields denoted by open diamonds, which meet the threshold criteria.

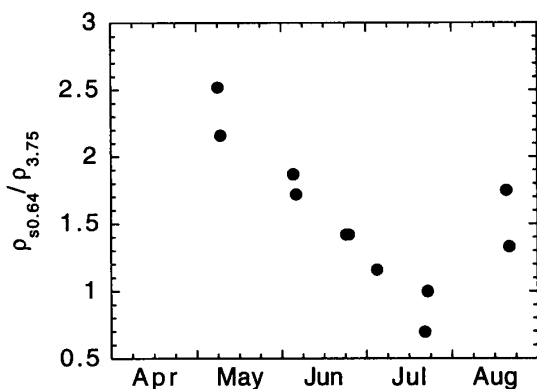


Fig. 12. Ratios of surface reflectance in the visible,  $\rho_{s0.64}$ , to mid-IR reflectance observed by satellite,  $\rho_{3.75}$ , for threshold criteria  $\rho_{3.75} < 0.025$ .

olds defined by only the darkest pixels. Thus, we define dark, dense vegetation to be those pixels with  $\rho_{3.75} < 0.025$ .

Fig. 11 shows the mean values of  $\rho_{0.64}$ ,  $\rho_{s0.64}$ , and  $\rho_{3.75}$  for the pixels that pass the thresholds for the two surface categories: forest and open fields. Fig. 11 also shows the fraction of the original pixels that pass the criteria. No pixels meet the criteria for April 21 or July 21. A very

small percentage of open field pixels meet the criteria for any date and these may actually be forest pixels erroneously identified due to errors in the registration. The ratios between the corrected surface reflectance in the visible,  $\rho_{s0.64}$  and the reflectance at  $3.75 \mu\text{m}$ ,  $\rho_{3.75}$ , from Fig. 11 are plotted in Fig. 12. Thus, the surface value of  $\rho_{s0.64}$  can be approximated by  $(1.5 \pm 0.5) \rho_{3.75}$ , where 1.5 is the mean of the points in Fig. 12 and the uncertainty 0.5 is the standard deviation. The small sample size and large standard deviation indicate the importance of verifying this relationship with subsequent data before application to global remote sensing of aerosol loading.

#### X. VEGETATION INDEX BASED ON THE MID-IR REFLECTANCE

We have shown that the reflectance in the  $3.75 \mu\text{m}$  channel,  $\rho_{3.75}$ , corrected for emission, is well correlated with  $\rho_{0.64}$  in each image. As a result, we can write a new normalized difference vegetation index that replaces the reflectance in the  $0.64 \mu\text{m}$  with the reflectance in the  $3.75 \mu\text{m}$  channel. The new index is defined as

$$\text{VI3} = (\rho_{\text{NIR}} - \rho_{3.75}) / (\rho_{\text{NIR}} + \rho_{3.75}) \quad \text{for } \rho_{\text{NIR}} \geq \rho_{\text{red}}$$

or

$$\text{VI3} = 0 \quad \text{for } \rho_{\text{NIR}} < \rho_{\text{red}} \quad (8)$$

where  $\rho_{\text{NIR}}$  is the reflectance in the near-IR AVHRR channel and  $\rho_{3.75}$  is the reflectance in the  $3.75 \mu\text{m}$  channel. The restrictions that  $\rho_{\text{NIR}} \geq \rho_{\text{red}}$  protects the index from being applied to water areas where the index is ill defined.

We do not intend in this paper to analyze this index, but rather to introduce briefly the concept. VI3 is a normalized index and will be less sensitive to bidirectional reflectance and subpixel clouds than  $\rho_{3.75}$  in the same manner that NDVI is superior to  $\rho_{0.64}$ . We have already demonstrated the advantage of using a mid-IR channel for forest detection and shown that the mid-IR is less sensitive to visibility (optical thickness) than the visible. Fig. 13 (a) compares the sensitivity of VI3 and NDVI to variations in haze and is analogous to Fig. 10 described in Section VIII. We see in this figure that indeed, VI3 is much less sensitive to haze than NDVI. It follows that for some applications, such as the detection of dark, dense vegetation in hazy conditions, VI3 may prove to be a superior vegetation index to NDVI.

For AVHRR, VI3 has the added advantage over NDVI and  $\rho_{3.75}$  of reduced sensitivity to water vapor absorption because both  $\rho_{0.64}$  and  $\rho_{3.75}$  are affected by water vapor, and this effect is reduced by the normalization in VI3. Fig. 13(b) demonstrates the reduced sensitivity of VI3 to water vapor absorption. In this figure, the solid curves denote the observed values of each variable, while the dashed curve shows the results of a simulation where the atmospheric profile is allowed to vary sinusoidally between tropical (humid) and winter mid-latitude (dry) conditions.

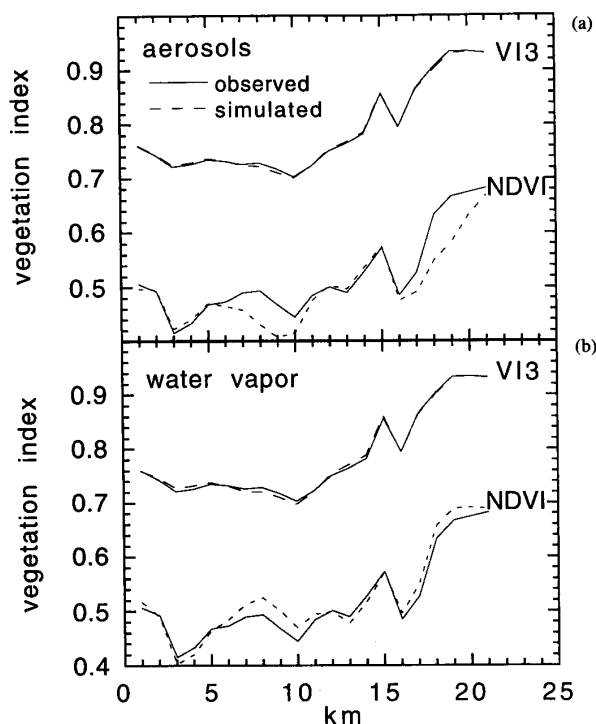


Fig. 13. Transect of PA site showing the values of VI3 and NDVI as a function of distance along the transect. The solid curves denote the observed AVHRR values. (a) The dashed curves denote the values resulting from a simulation using the 5S radiative transfer model with a sinusoidally varying visibility. Visibility ranges from 10 to 35 km with a period equal to one half the transect length. (b) The dashed curves denote the values resulting from a simulation with an atmosphere varying sinusoidally from mid-latitude winter to tropical conditions.

## XI. SUMMARY AND DISCUSSION

The mid-IR spectral channels on the planned MODIS-EOS sensor ( $3.75$  and  $3.95 \mu\text{m}$ ) and on-board the AVHRR provide a unique opportunity for the remote sensing of vegetation in general and the presence of forest in particular. Though this paper develops a method to locate forested pixels used in the remote sensing of aerosol, the method has further reaching implications. Surface reflectance in the  $3.75 \mu\text{m}$  channel is highly correlated with the reflectance in the red ( $0.64 \mu\text{m}$ ) channel. Presence of vegetation, moisture in soil, and complex vegetation structure that increases shadowing and photon trapping, darken both of the channels. But while the red channel is strongly affected by aerosol scattering, the  $3.75 \mu\text{m}$  is transparent to most aerosol types except for dust. Even independent of the presence of aerosol, the reflectance in  $3.75 \mu\text{m}$ ,  $\rho_{3.75}$ , was shown to be more sensitive than the reflectance at  $0.64 \mu\text{m}$  and NDVI to the presence of forest and separate it better from open field regions. Based on the results it can be proposed that for the remote sensing of aerosol over dark, dense vegetation the dense forest pixels can be determined for  $\rho_{3.75} < 0.025$ . On the other hand,  $\rho_{3.75}$  did not show the seasonal variation in the vegetation of the open fields that was observed by the  $\rho_{0.64}$ . This may be

due to either a seasonal variation in surface emissivity or simply the fact that the visible and mid-IR spectral ranges measure different vegetation phenomena.

The  $3.75 \mu\text{m}$  channel has two major advantages: it penetrates haze and it is extremely sensitive to liquid water in vegetation. The most important limitation of the  $3.75 \mu\text{m}$  channel is the necessity of correcting for emission and the assumption of the surface emissivity at  $11 \mu\text{m}$ . Furthermore, the  $3.75 \mu\text{m}$  channel is limited in that  $\rho_{3.75}$  will be sensitive to surface liquid water such as recent rain puddles, swamps, lakes, and rivers. The  $2.1 \mu\text{m}$  channel, which will be available on MODIS, also penetrates most haze types, and has the advantage of not having a significant emission component, thereby eliminating the need to assume a surface emissivity. However, the  $2.1 \mu\text{m}$  channel is less sensitive to liquid water. Investigation is necessary to determine the practicality of using radiation at  $2.1 \mu\text{m}$  to detect vegetation.

Because of the properties of  $\rho_{3.75}$ , we propose a new vegetation index, VI3, in which the red channel in the NDVI is replaced with the reflective part of the  $3.75 \mu\text{m}$  channel expecting that VI3 will also be less sensitive to haze. However, because of the  $3.75 \mu\text{m}$  channel's limitations, global monitoring of vegetation with VI3 is doubtful. VI3 is recommended for detection of forests. VI3 should be useful for the determination and classification of vegetation in areas that are covered by dense smoke or industrial/urban pollution.

## ACKNOWLEDGMENTS

The authors wish to thank M. Verstraete for his careful review of the paper and his supportive, constructive criticisms. They also wish to acknowledge B.-C. Gao, E. Vermote, and an anonymous reviewer who made several helpful suggestions after reviewing an earlier version of this paper. A. Arking and J. Merritt provided the AVHRR images and computer support, and M. Murthy helped in classifying the pixels with the U.S. Geological Survey topographical maps. Thank you goes to A. Mattoo for help with the word processing.

## REFERENCES

- [1] Arking, A. and J. D. Childs, "Retrieval of cloud cover parameters from multispectral satellite images," *J. Clim. App. Met.*, vol. 24, pp. 322-333.
- [2] J. A. Coakley, Jr., R. L. Bernstein, and P. A. Durkee, "Effect of ship stack effluents on cloud reflectance," *Science*, vol. 237, pp. 953-1084, 1987.
- [3] R. S. Fraser and Y. J. Kaufman, "The relative importance of scattering and absorption in remote sensing," *IEEE Trans. Geosci. Rem. Sens.*, vol. 23, pp. 625-633, 1985.
- [4] D. M. Gates, *Biophysical Ecology*, New York: Springer-Verlag, 1980, pp. 1-611.
- [5] G. Gesell, "An algorithm for snow and ice detection using AVHRR data: An extension to the APOLLO software package," *Int. J. Remote Sensing*, vol. 10, pp. 897-905, 1989.
- [6] S. N. Goward, C. J. Ticler, and D. G. Dye, "North American vegetation patterns observed with the NOAA-7 advanced very high resolution radiometer," *Vegetatio*, vol. 64, pp. 3-14, 1986.
- [7] J. E. Hansen and L. D. Travis, "Light scattering in planetary atmospheres," *Space Sci. Rev.*, vol. 16, pp. 527-610, 1974.
- [8] B. N. Holben, "Characteristics of maximum value composite images

- for temporal AVHRR data," *Int. J. Rem. Sens.*, vol. 7, pp. 1417-1437, 1986.
- [9] B. N. Holben and R. S. Fraser, "Red and near infrared response to off nadir viewing," *Int. J. Rem. Sens.*, vol. 5, pp. 145-160, 1984.
- [10] B. Holben, E. Vermote, Y. J. Kaufman, D. Tanré, and V. Kalb, "Aerosol retrieval over land from AVHRR data—Application for atmospheric correction," *IEEE Trans. Geosci. Rem. Sens.*, vol. 30, pp. 212-232, 1992.
- [11] A. R. Huete, "A soil-adjusted vegetation index (SAVI)," *Rem. Sens. Environ.*, vol. 25, pp. 295-309, 1988.
- [12] W. M. Irvine and J. B. Pollack, "Infrared optical properties of water and ice spheres," *Icarus*, vol. 8, pp. 324-360, 1968.
- [13] Y. J. Kaufman, "The atmospheric effect on remote sensing and its correction," in *Optical Remote Sensing, Technology and Application*, G. Asrar, Ed. New York: Wiley, Ch. 9, 1989.
- [14] Y. J. Kaufman and R. S. Fraser, "Light extinction by aerosol during summer air pollution," *J. Appl. Meteorol.*, vol. 22, pp. 1694-1706, 1983.
- [15] Y. J. Kaufman and T. Nakajima, "Effect of Amazon smoke on cloud microphysics and albedo," *J. Appl. Meteorol.*, vol. 32, pp. 729-744, 1993.
- [16] Y. J. Kaufman and C. Sendra, "Algorithm for automatic atmospheric corrections to visible and near-IR satellite imagery," *Int. J. Rem. Sens.*, vol. 9, pp. 1357-1387.
- [17] Y. J. Kaufman, D. Tanré, B. N. Holben, B. Markham and A. Gitelson, "Atmospheric effects on the NDVI—Strategies for its removal," in *Proc. IGARSS'92*, 1992, pp. 1238-1241.
- [18] Y. J. Kaufman, A. Setzer, D. Ward, D. Tanré, B. N. Holben, P. Menzel, M. C. Pereira, and R. Rasmussen, "Biomass burning airborne and spaceborne experiment in the Amazonas (BASE-A)," *J. Geophys. Res.*, 1992.
- [19] Y. J. Kaufman and D. Tanré, "Atmospherically resistant vegetation index (ARVI) for EOS-MODIS," *IEEE Trans. Geosci. Rem. Sens.*, vol. 30, pp. 261-270, 1992.
- [20] M. D. King, Y. J. Kaufman, W. P. Menzel, and D. Tanré, "Remote sensing of imaging spectrometer (MODIS)," *IEEE Trans. Geosci. Rem. Sens.*, Vol. 30, pp. 2-27, 1992.
- [21] J. Labed and M. P. Stoll, "Angular variation of land surface spectral emissivity in the thermal infrared: laboratory investigations on bare soils," *Int. J. Rem. Sens.*, vol. 12, pp. 2299-2310, 1991.
- [22] J. Malingreau and C. J. Tucker, "Large scale deforestation in the southeastern Amazon basin of Brazil," *Ambio*, vol. 17, pp. 49-55, 1988.
- [23] T. Nakajima, M. D. King, J. D. Spinhirne, and L. F. Radke, "Determination of the optical thickness and effective particle radius of clouds from reflected solar radiation measurements, Part II: Marine stratocumulus observations," *J. Atmos. Sci.*, vol. 48, pp. 728-750, 1991.
- [24] S. E. Nicholson, M. L. Davenport, and A. D. Malo, "A comparison of the vegetation response to rainfall in the Sahel and east Africa, using NDVI from NOAA AVHRR," *Climate Change*, vol. 17, pp. 209-214, 1990.
- [25] B. Pinty and M. M. Verstraete, "GEMI: A non-linear index to monitor global vegetation from satellites," *Vegetatio*, 1992.
- [26] I. Ruff and A. Gruber, "Multispectral identification of clouds and earth surfaces using AVHRR data," in *Proc. 5th Conf. Atmos. Radiat.*, Baltimore, MD, Oct. 31-Nov. 4, 1983, AMS, pp. 475-478.
- [27] J. W. Salisbury, D. M. D'Aria, and L. E. Brown, "Infrared (2.08-14  $\mu\text{m}$ ) spectra of soils: A preliminary report," 1990.
- [28] P. J. Sellers, "Canopy reflectance, photosynthesis and transpiration," *Int. J. Rem. Sens.*, vol. 6, pp. 1335-1372, 1985.
- [29] D. Tanré, C. Deroo, P. Duhant, M. Herman, J. J. Morcrette, J. Perbos, and P. Y. Deschamps, "Description of a computer code to simulate the satellite signal in the solar spectrum," *Int. J. Rem. Sens.*, vol. 11, pp. 659-668, 1990.
- [30] D. Tanré, B. N. Holben, and Y. J. Kaufman, "Atmospheric correction algorithm for NOAA-AVHRR products: Theory and applications," *IEEE Trans. Geosci. Rem. Sens.*, vol. 30, pp. 231-248, 1992.
- [31] S. E. Taylor, "Measured emissivity of soils in the southeast United States," *Rem. Sens. Environ.*, vol. 8, pp. 359-364, 1979.
- [32] C. J. Tucker, I. Y. Fung, C. D. Keeling, and R. H. Gammon, "Relationship between atmospheric CO<sub>2</sub> variations and a satellite derived vegetation index," *Nature*, vol. 319, pp. 195-199, 1986.
- [33] C. J. Tucker, B. N. Holben, and T. E. Goff, "Intensive forest clearing in Rondonia, Brazil, as detected by satellite remote sensing," *Rem. Sens. Environ.*, vol. 15, p. 255, 1984.
- [34] M. M. Verstraete and B. Pinty, "The potential contribution of satellite remote sensing to the understanding of arid lands processes," *Vegetatio*, vol. 91, pp. 59-72, 1991.
- [35] K. T. Whitby, "The physical characteristics of sulfur aerosols," *Atmos. Environ.*, vol. 12, pp. 135-159, 1978.
- [36] W. L. Wolfe and G. J. Zissis, *The Infrared Handbook*, Washington, D.C.: Environ. Instit. Michigan, Office Naval Res., Dep. Navy, 1978.



**Yoram J. Kaufman** received the B.Sc. and M.Sc. degrees in physics from the Technion-Israel Institute of Technology, Haifa, Israel, in 1972 and 1974, respectively, and the Ph.D. degree from the Tel-Aviv University in 1979.

He is presently with the NASA Goddard Space Flight Center, Greenbelt, MD, where he began in 1979 on an NRC fellowship award. His current work includes theoretical and experimental research in atmosphere science, radiative transfer, and remote sensing. His research activities include remote sensing of aerosol and clouds, atmospheric correction of satellite imagery of the Earth's surface, interaction of aerosols and clouds, and their climatic impact, remote sensing of emissions from biomass burning in the tropics, and calibration of satellite sensors. He conducts field experiments that include measurements from aircraft and the ground of the aerosol properties (smoke aerosol, dust, and anthropogenic aerosol) and their effect on radiative transfer. He is a member of the Earth Observing System—MODIS team. Three of his papers on properties of CO<sub>2</sub> lasers and saturable absorbers, written from his work at Technion, were selected for the SPIE Milestone Series "of outstanding papers from the world literature on optical and optoelectronic science, selected papers on CO<sub>2</sub> lasers."



**Lorraine A. Remer** received the B.S. degree in Atmospheric Science from the University of California, Davis, in 1980, the M.S. degree in Oceanography from the University of California, San Diego—Scripps Institution of Oceanography in 1983 and the Ph.D. degree from the University of California, Davis in Atmospheric Science in 1991.

She spent three years working as a consultant, providing information and assistance to the wind energy industry in California. Currently, she is with Science Systems and Applications Inc., Lanham, MD, pursuing research in remote sensing of aerosols, atmospheric correction of satellite imagery, and aerosol-cloud interaction. Her research includes both theoretical simulations of radiative transfer and field experiments. She participated in recent field experiments that used remote sensing of dust aerosol over a desert transition zone and remote sensing and *in situ* measurements of sulfate aerosols and clouds over the eastern seaboard of the United States.